On-chip loss-modulated photonic topological edge states in anti-$\mathcal{PT}$-symmetric waveguide arrays

Zhihua Deng, Dingshan Gao,* Jianji Dong, and Xinliang Zhang
Wuhan National Laboratory for Optoelectronics, Huazhong University of Science and Technology, Wuhan 430074, China

(Received 7 May 2023; revised 23 July 2023; accepted 3 August 2023; published 6 October 2023)

Non-Hermiticity has emerged as a promising tool to induce topological phase transitions, allowing for the design of tunable and functional topological devices such as topological lasers and switches on on-chip integrated optical platforms. In this work, we experimentally demonstrate loss-modulated photonic topological edge states in anti-parity-time-symmetric waveguide arrays. Loss is introduced via carefully designed subwavelength grating (SWG) waveguides, allowing for on-chip control of topological responses. Our results show that loss not only induces topological phase transition but also enhances topological responses, leading to the increased localization of topological edge states and the anomaly reduced intrinsic loss of the topological edge states. Our work provides a platform based on SWG waveguides for exploring non-Hermiticity-induced photonic topological responses and corresponding applications.

DOI: 10.1103/PhysRevApplied.20.044019

I. INTRODUCTION

Topological insulating phases have been a hot research topic in physics [1–4] over the past decades. In Hermitian systems, they enable many alternative phenomena and promise various future applications, such as unidirectional waveguides [5], robust quantum computation [6], four-dimensional quantum Hall effect [7], and more. Additionally, interfacing non-Hermitian and topological physics can result in even richer topological responses [8,9].

One example of this is the non-Hermitian skin effect [10], which is typically induced by anisotropic coupling and has been utilized for a highly efficient funnel for light [11]. Another example is the use of open systems with gain and/or loss, such as the selective enhancement of topological edge states [12], parity-time-symmetric topological interface states [13], hybrid skin-topological effect [14,15], non-Hermiticity amplified edge states used for topologically protected lasers against disorder and defects [16–19], among others.

Recent theoretical studies have shown that gain and loss can solely induce topological insulating phases and higher-order topological corner states [20–27], leading to non-Hermitian topological responses with well-defined topological invariants. These responses have been experimentally observed in acoustic crystals [28,29], electrical circuits [30], elastic metamaterials [31], and thermal diffusion systems [32], where on-site gain and/or loss were engineered in modified Benalcazar-Bernevig-Hughes and tetratomic Su-Schrieffer-Heeger (SSH) models. However, there have been no relevant optical experiments so far. In integrated photonics, gain and loss can be introduced in a controllable manner [16–18,33], making the realization of non-Hermiticity-induced photonic topological phase transitions and topological edge states of great interest for the development of tunable functional photonic topological devices [34], such as topological lasers and optical switches.

In this work, we present our design and experimental demonstration of loss-modulated photonic topological edge states in anti-parity-time-symmetric waveguide arrays. The losses are introduced using subwavelength grating (SWG) waveguides, which can be fabricated on a silicon chip using a single-step etching process. Our simulations and photonic measurements show that the topological responses are solely induced by loss. When there is no loss, the array behaves as a trivial SSH model with an insulating band gap and no edge states. As the loss increases and passes through the topological phase transition point, the SSH model becomes a tetratomic SSH model and the insulating gap gradually closes and reopens a topological insulating gap, in which topological edge states emerge. Interestingly, further increasing the loss leads to an enhanced degree of localization of the topological edge states, and a reduction in their intrinsic loss.

II. MODEL AND THEORY

We explore a one-dimensional passive tetratomic non-Hermitian SSH model, as shown in Fig. 1(a), which describes a coupled single-mode waveguide array. All the

*dsgao@hust.edu.cn

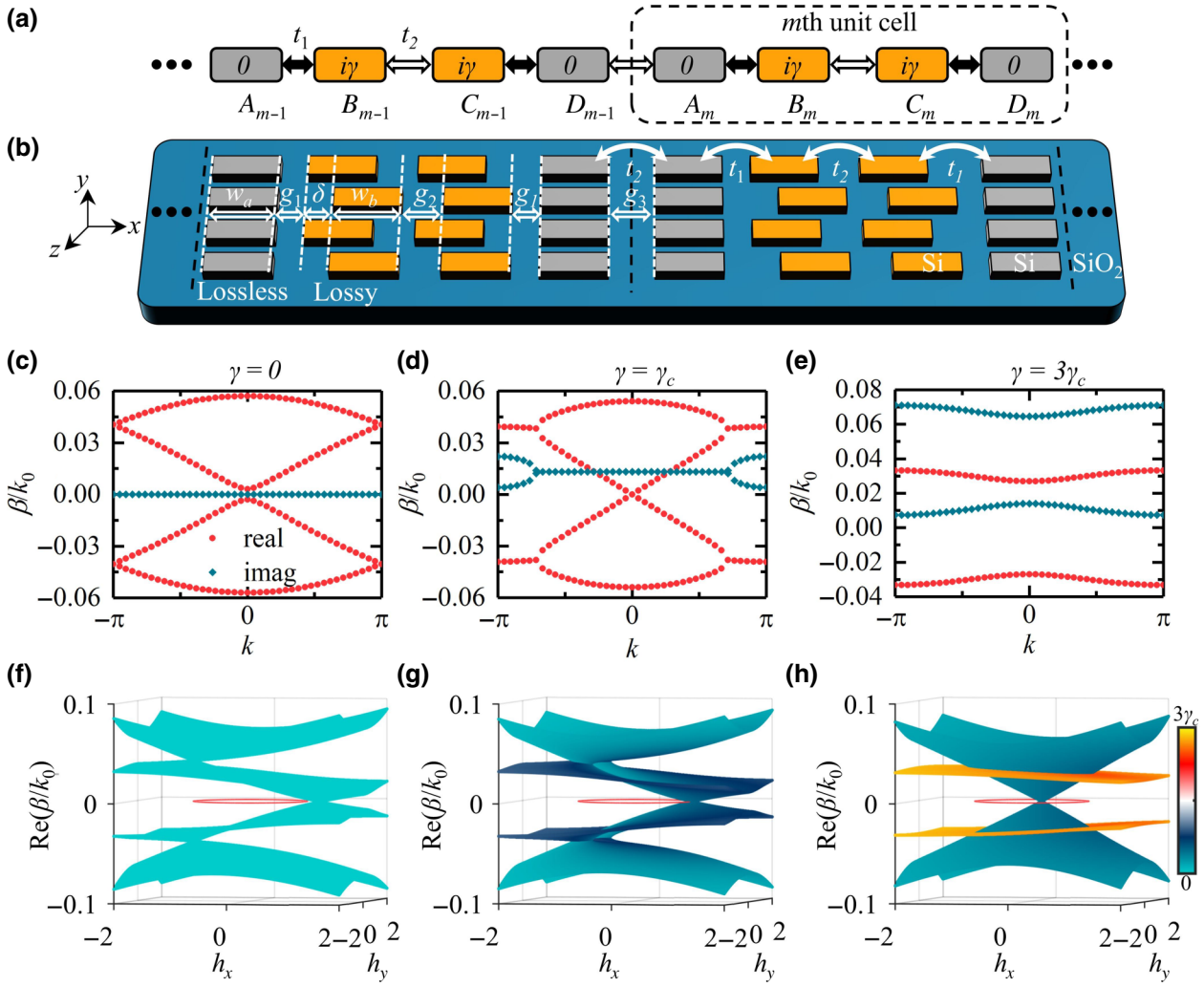

FIG. 1. Loss-induced photonic topological phase transition and the photonic implementation. (a) Schematic of the anti-parity-time-symmetric non-Hermitian SSH model. (b) Illustration of the SWG waveguide array. The lossless SWGs are colored in gray and the lossy SWGs are colored in yellow. (c)–(e) Band structures of the SWG array for $\gamma = 0$ (c), $\gamma = \gamma_c$ (d), and $\gamma = 3\gamma_c$ (e), with $t_1/k_0 = 0.03$ and $t_2 = 0.9t_1$, where $k_0 = 2\pi/\lambda$ is propagation constant in vacuum, $\lambda = 1550$ nm and $\gamma_c = 0.0262k_0$. The real part of energy is colored in red and the imaginary part of energy is colored in cyan. (f)–(h) Complex band structures in the two-dimensional parameter space (h_x, h_y) for $\gamma = 0$ (f), $\gamma = \gamma_c$ (g) and $\gamma = 3\gamma_c$ (h), with $t_1/k_0 = 0.03$, $t_2 = 0.9t_1$, where the value indicates the real part and the color indicates the imaginary part of the energy. The unit circle on the zero-energy surface is marked by a red circle.

waveguides are designed with the same effective propagation constant, which can be taken equal to a reference zero energy. The coupling coefficients t_1 and t_2 are determined by the distance between adjacent waveguides. The on-site potential profile $(0, i\gamma, i\gamma, 0)$ with inversion symmetry is introduced to the tetratomic unit cell, where positive coefficients mean loss in the waveguide. This tight-binding model is the passive version of the model in a theoretical paper [25].

Through the coupled-mode theory (CMT), this tight-binding model can be realized by the precisely designed SWG waveguide array on a silicon-on-insulator (SOI) chip [35], as shown in Fig. 1(b). The advantage of SWG waveguides is that the coupling coefficients, effective propagation constants and loss coefficients can be precisely controlled. Non-Hermitian systems constructed from SWG waveguides have already been utilized to realize chiral mode switching by encircling exceptional points [36,37]. Compared with the conventional method of introducing propagation loss by adding metals on silicon waveguides, where the over-lay process is inevitable [38], taking advantage of SWG waveguides will avoid the complicated nanofabrication process, and only a single-step etching process is required [36,37]. The SWG waveguide array is fabricated by patterning the top Si layer of a SOI wafer. The period of lossless SWG waveguides is fixed as 300 nm, which is smaller than the Bragg period. As shown in Fig. 1(b), the lossy SWG waveguides are formed by introducing a

corrugation amplitude δ. As the lossy SWG is periodically corrugated, its period is twice that of the lossless SWG and larger than the Bragg period. Therefore, light-field energy in lossy SWG waveguides will radiate to the substrate and air cladding, resulting in propagating loss [37]. The effective propagation constant can be adjusted by tuning width w_a and w_b, and the loss of the lossy SWG waveguide can be smartly adjusted by tuning δ. The height in the y direction and the filling factor in the z direction of SWG waveguides are set as 220 nm and 0.565, respectively. To ensure that only the fundamental transverse electric (TE) mode is allowed, w_b is fixed as 700 nm. In the design of the topological waveguide array, we obtain the desired loss by adjusting corrugation amplitude δ, then match the propagation constants of lossless and lossy SWG by adjusting w_a, and finally achieve the desired coupling coefficient distribution by adjusting the spacings g_1, g_2, and g_3.

The band structure and topology of the tight-binding model or the SWG waveguide array is associated with the non-Hermitian Bloch Hamiltonian

$$H_k = \begin{bmatrix} 0 & t_1 & 0 & t_2 e^{-ik} \\ t_1 & i\gamma & t_2 & 0 \\ 0 & t_2 & i\gamma & t_1 \\ t_2 e^{ik} & 0 & t_1 & 0 \end{bmatrix}, \tag{1}$$

where k is the wave number in the Brillouin zone. H_k is anti-parity-time- (APT) symmetric, i.e., $(PT)H_k(PT)^{-1} = -H_k$, where $P = i\sigma_x \otimes \sigma_y$, T is the complex-conjugation operation, and σ_i refers to the Pauli matrix. H_k also has TRS†, PHS†, and chiral symmetry (see Sec. I within the Supplemental Material [39] for details). Therefore, H_k belongs to the BDI† class in the 38-fold topological classifications of non-Hermitian systems [8]. According to these symmetries of the Hamiltonian, some properties and topology of energy bands can be directly obtained. In fact, H_k has four complex energy bands. The APT symmetry ensures the energies in pairs with identical imaginary part and opposite real part, and the TRS† ensures the energy bands are symmetric about $k = 0$. Moreover, for Hamiltonian belonging to BDI† classification, the topological phase transition is characterized by the closing and reopening of the real part of the energy bands, which is helpful for us to judge the topological phase transition process. The four energy bands of our tetratomic non-Hermitian Hamiltonian are

$$\beta_{\pm,\pm} = \frac{i\gamma}{2} \pm \sqrt{t_1^2 + t_2^2 - \left(\frac{\gamma}{2}\right)^2 \pm 2t_2\sqrt{t_1^2\cos^2\frac{k}{2} - \left(\frac{\gamma}{2}\right)^2}}. \tag{2}$$

The interplay between the couplings and the non-Hermiticity alters the band and will generate the nontrivial topology [25]. In the following discussion, the coupling coefficients are fixed as $t_1/k_0 = 0.03$, and $t_2 = 0.9t_1$, where $k_0 = 2\pi/\lambda$ is propagation constant in vacuum and $\lambda = 1550$ nm. In the absence of loss ($\gamma = 0$), the model is a trivial Hermitian SSH model with an insulating band gap [35,40], as shown in Fig. 1(c). Moreover, the increase of loss will give rise to the closure and reopening of the real energy bands, as shown in Figs. 1(c)–1(e). In particular, in the center of the Brillouin zone ($k = 0$), the insulating band gap will be closed at a critical point γ_c, labeling the topological phase transition point, as shown in Fig. 1(d). Constrained by APT symmetry and TRS†, the topological phase transition occurs at $\beta_{\pm,\pm} = 0$ and $k = 0$. Hence the critical point γ_c can be derived from $(\gamma_c/2)^2 + t_2^2 = t_1^2$, and equals $0.0262k_0$.

The band topology of the APT-symmetric Hamiltonian relates to the geometry of the Bloch Hamiltonian winding around the degenerate points in a two-dimensional parameter space through replacing $e^{\pm ik}$ by $h_x \pm ih_y$ [25]. The k-dependent Bloch Hamiltonian H_k corresponds to a unit circle $h_x^2 + h_y^2 = 1$ in the two-dimensional parameter space (h_x, h_y). When the energy bands in Figs. 1(c)–1(e) are extended to the two-dimensional parameter space (h_x, h_y), the complex energy bands in Figs. 1(f)–1(h) are obtained. The topology is determined by the degenerate point (DP) winding around the unit circle with zero energy. As shown in Fig. 1(f), the DP is outside the red unit circle, indicating that winding number equals zero and the model is in trivial insulating phase. For $\gamma = \gamma_c$ in Fig. 1(g), the DP locates on the red unit circle, implying topological phase transition point. Further increasing the non-Hermiticity, as shown in Fig. 1(h), the DP is enclosed in the red unit circle, indicating topological nontrivial phase and winding number equaling one. From the properties of eigenvalue of the energy bands in parameter space, we have obtained the topological properties as have been predicted by bands in k space. Moreover, from the properties of eigenvectors of the energy bands in k space, band topology can be also obtained from integer partial global Zak phase [25], which is equal to geometric winding number multiplied by π (see Sec. II within the Supplemental Material [39] for details).

III. LOSS-MODULATED PHOTONIC TOPOLOGICAL EDGE STATES

As a consequence of the nontrivial topology, the bulk-edge-correspondence makes sure there exist one pair of identical topological edge states at the boundary of the waveguide array in the topologically nontrivial phase [8,25]. It should be noted that even in the case of open boundary condition, the system Hamiltonian still supports the symmetry mentioned above (see Sec. I within the Supplemental Material [39] for details), such as the APT symmetry. The APT symmetry ensures that the real parts of the two edge states are fixed at zero energy, and the imaginary parts of the two edge states are the same. The eigenspectrum of the finite APT-symmetric waveguide array in

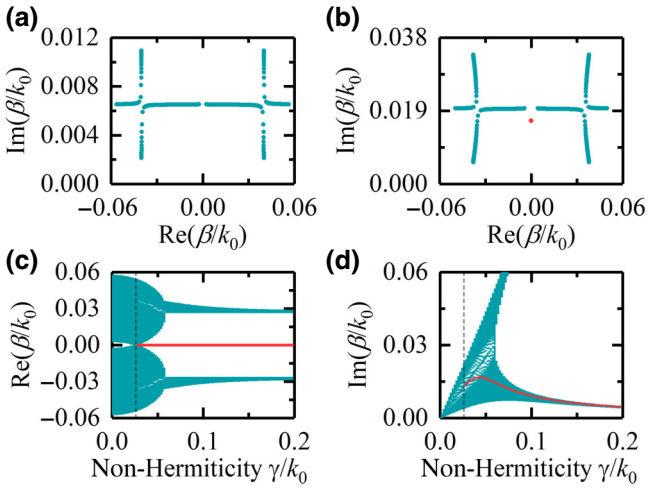

FIG. 2. Eigenspectrum of the finite APT-symmetric waveguide array in topologically trivial ($\gamma = 0.5\gamma_c$) and nontrivial ($\gamma = 1.5\gamma_c$) regions are plotted in the complex plane, as shown in (a) and (b), respectively. The real part and the imaginary part of the eigenspectrum for the finite APT-symmetric waveguide array with varying non-Hermiticity are shown in (c) and (d), respectively. In (a)–(d), the edge states are marked by red, and the bulk states are marked by cyan. The topological phase transition point γ_c is identified by the gray dotted line in (c) and (d).

topologically trivial and nontrivial regions are plotted in the complex plane, as shown in Figs. 2(a) and 2(b), respectively. In the topologically trivial phase, there is only a trivial band gap in the real part of the energy band, while, in the topologically nontrivial phase, there is a nontrivial band gap in the real part of the energy band that supports a pair of topological zero modes with the same loss. The eigenspectrum of the finite APT-symmetric waveguide array varying with the non-Hermiticity is also plotted. As shown in Fig. 2(c), the edge states marked by red solid lines, appear only at $\gamma \geq \gamma_c$, and are fixed at zero energy in the topological band gap. The red solid line in Fig. 2(d) shows the intrinsic loss of the edge states. The intrinsic loss first increases with the increase of non-Hermiticity, and then anomaly decreases after the non-Hermiticity crossing a certain threshold ($\gamma/k_0 \approx 0.044$). At present, this phenomenon is difficult to explain unless we show the eigenfield distribution of the edge states.

The eigenfield on the left side of the open boundary in the mth unit cell can be written as $|\psi_{m,L}\rangle = \chi^{m-1}\{1, i\lambda/t_1, -\chi t_2/t_1, 0\}$, where $\chi = -\lambda/(\lambda - \gamma)$ and λ represents the intrinsic loss of the current edge state (see Sec. III within the Supplemental Material [39] for detailed derivation). The right edge state $|\psi_{m,R}\rangle$ is the mirror reflection of the left edge state $|\psi_{m,L}\rangle$, and the same analysis can be carried out. So, we focus on the edge states $|\psi_{m,L}\rangle$ on the left boundary. According to the naming of the waveguides in Fig. 1(a), the field in the unit cell is mainly distributed on the lossless A_m waveguide, but there is also certain distribution on the two lossy waveguides B_m and C_m. There is no distribution on the lossless D_m waveguide. The field distribution characteristics within each unit cell are the same, and the amplitude attenuation between adjacent cells is determined by χ. The relationship between χ and non-Hermiticity γ can be obtained numerically, and the larger the non-Hermiticity γ is, the smaller the χ is (see Sec. III within the Supplemental Material [39] for details). This shows that with the increase of the non-Hermiticity γ, the field becomes more localized at the boundary. When the non-Hermiticity γ is small, the distribution of edge state is relatively wide, and the field is distributed more on the lossy waveguide. Therefore, with the increase of the non-Hermiticity γ, the intrinsic loss of the edge state will initially increase. However, further increasing the non-Hermiticity γ, the edge state becomes more localized, and the distribution on the lossy waveguide is less and less. In addition, the edge state is mainly distributed on the lossless waveguide closest to the boundary (A_1 waveguide). Therefore, the non-Hermiticity induced optical field localization reduces the loss of edge states. By analyzing the eigenvalues and eigenfields of waveguide array, it is found that the non-Hermiticity γ can well modulate the localization and intrinsic loss of topological edge states.

We also study the influence of two kinds of disorder on topological edge states (see Sec. IV within the Supplemental Material [39] for details). The first kind of disorder is related to the actual process error, for example, the width error of each waveguide. The coupling coefficients and loss coefficients change as a whole, which is not random. Therefore, such disorder will not break the original symmetry, and zero-energy edge states exist stably in the band gap. In the second case, we consider the influence of random disorder by randomly affecting some coupling coefficients and loss coefficients in the array. The disorder strength is characterized by η, ranging from 0 to 1. When η is greater than 0 and less than 0.5, the original symmetry almost disappears. The edge states still exist in the band gap, showing robustness, but are no longer stable at zero energy. Further increasing η, the band gap gradually closes, and the edge states are finally submerged in the bulk states.

IV. SIMULATION AND VERIFICATION

In the following, we will carry out finite-difference time-domain (FDTD) simulations to study the modulation effect of loss on edge states through the evolution characteristics of mode fields. Here, we set the number of waveguides of the finite waveguide array to 16, and the length of the waveguide array to 36 μm. The values of w_a, g_1, g_2, and g_3 under different non-Hermiticity (determined by δ) involved in this study are listed in Sec. V within the Supplemental Material [39].

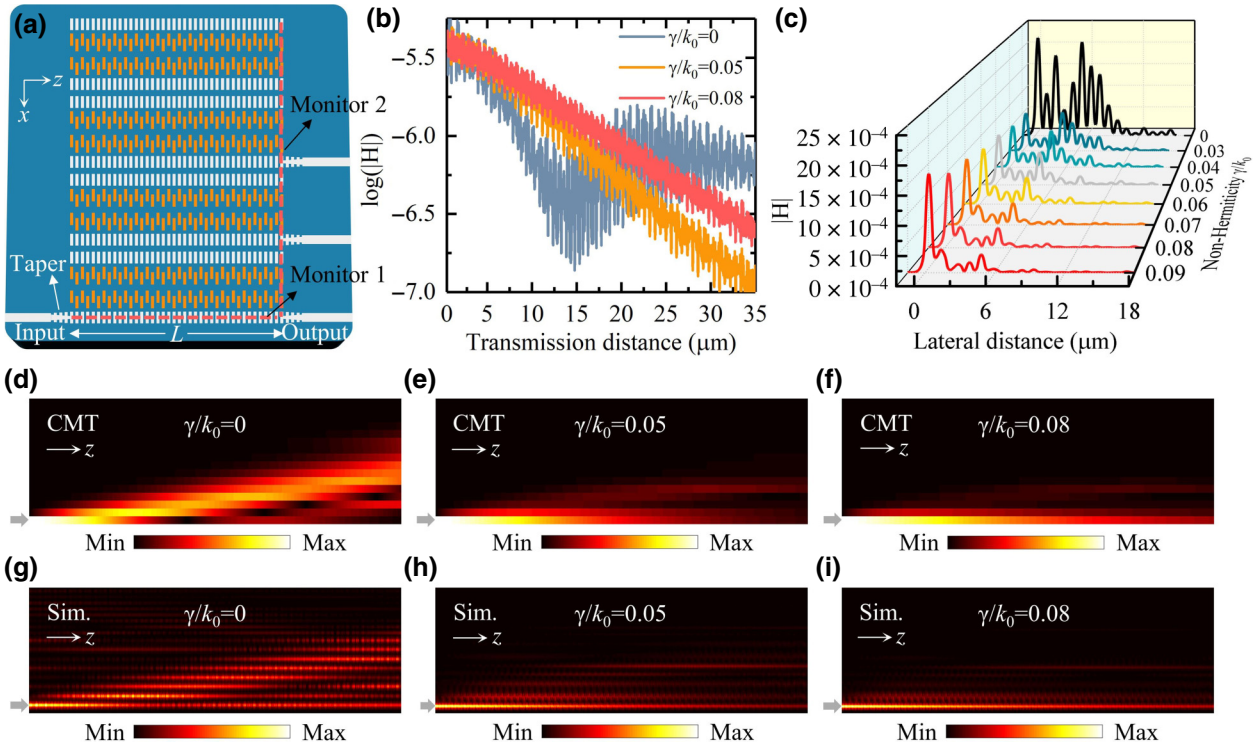

FIG. 3. FDTD simulation results of the finite APT-symmetric waveguide array. (a) The schematic of the finite APT-symmetric waveguide array. The positions of monitors 1 and 2 are marked by red dotted lines. The lossless single-mode waveguides, tapers and SWG waveguides are colored in white. The lossy SWG waveguides are colored in yellow. (b) Evolution of the magnetic field on monitor 1. (c) The lateral field distribution at the output of waveguide array on monitor 2. Field evolution calculated by CMT are shown in (d)–(f) for $\gamma/k_0 = 0, 0.05$, and 0.08, respectively. Field evolution based on FDTD simulations are shown in (g)–(i) for $\gamma/k_0 = 0, 0.05$, and 0.08, respectively.

The schematic of the finite waveguide array model is shown in Fig. 3(a). The light enters the outermost single-mode waveguide to excite the topological edge states of the waveguide array via a taper. A field detector (monitor 1) is placed in the middle of the lowest waveguide to monitor the evolution characteristics of the magnetic field. Although the eigenmode of single-mode waveguide does not completely match the eigenmode of the edge state, the mode-field transmission attenuation characteristics are very similar with varying γ after the excitation by these two eigenmodes. And the greater the γ, the closer the two attenuation characteristics are (see Sec. VI within the Supplemental Material [39] for details). Therefore, we can judge the topological phase transition through the field attenuation characteristics of monitor 1. In the trivial phase of the system ($\gamma = 0$), the light field diffracts into the waveguide array and partially returns to the lowest waveguide [35,40]. As depicted by the gray line in Fig. 3(b), the magnetic field in the lowest waveguide first diffracts into the array, causing the field amplitude to decrease. Then, part of the optical field couples back, and the amplitude increases. In contrast, when the system is in the nontrivial phase, the evolution is distinct, as shown by the yellow ($\gamma/k_0 = 0.05$) and red ($\gamma/k_0 = 0.08$) lines in Fig. 3(b). The magnetic fields decrease exponentially (linear attenuation under logarithm). The attenuation is slower when γ is larger, indicating that the intrinsic loss of the corresponding edge state is lower, as previously predicted.

However, monitor 1 cannot directly monitor the impact of non-Hermiticity on the localization degree of the edge states. Therefore, another field detector (monitor 2) is placed at the end of the waveguide array to monitor the final field characteristics after mode field evolution. As illustrated in Fig. 3(c), as the loss increases, the mode field are gradually localized at the boundary, indicating an enhanced degree of localization of the edge states. Moreover, the field amplitude on the lowest waveguide gradually increases after the transition point, suggesting a reduced intrinsic loss of the edge states.

To observe the field evolution in the waveguide array excited by a single waveguide, theoretical results based on CMT are presented in Figs. 3(d)–3(f) for $\gamma/k_0 = 0$, 0.05, and 0.08, respectively. Corresponding optical results based on FDTD are also shown in Figs. 3(g)–3(i). These figures reveal that the optical results are in excellent agreement with the CMT results, and they clearly demonstrate the topological transition induced by non-Hermiticity γ, as well as the enhanced degree of localization of the edge

states resulting from non-Hermiticity γ. As a comparison, we also perform simulations utilizing bulk excitation to generate bulk states without any localized properties (see Sec. VI within the Supplemental Material [39] for details).

V. ON-CHIP EXPERIMENTAL REALIZATION

To experimentally observe the loss-modulated topological edge states, we fabricated APT-symmetric SWG waveguide arrays on a SOI chip through a single-step etching process [36,37]. Figure 4(a) shows the top-view SEM images of two of our fabricated structures with non-Hermiticity γ/k_0 of 0 and 0.08. The insets depict the corresponding two kinds of unit cells, where the lossless and lossy SWG waveguides are clearly identifiable. The structures fabricated in the experiments agree well with the designed structures in simulations.

The transmission properties of the fabricated APT-symmetric SWG waveguide arrays are measured. In experiments, the light enters the chip from the amplified spontaneous emission (ASE) source through the focusing grating coupler and enters the array through the lowest waveguide. In practice, the output optical field signal is detected by three A-type waveguides, as shown in Fig. 4(a). The lowest waveguide is the A_1 waveguide. In combination with the eigenfield of the SWG waveguide array, the optical field will be mainly concentrated in $A_{1,2,3}$ waveguides. Therefore, three output waveguides are connected to three types of A waveguides as outputs to detect the optical transmission spectrum, which is measured by an optical spectrum analyzer (OSA) through the output focusing grating coupler. It should be mentioned that, although the device is designed to operate at 1550 nm, a slight variation in couplings and losses (through the change of wavelength) will not affect topological features. Consequently, the device

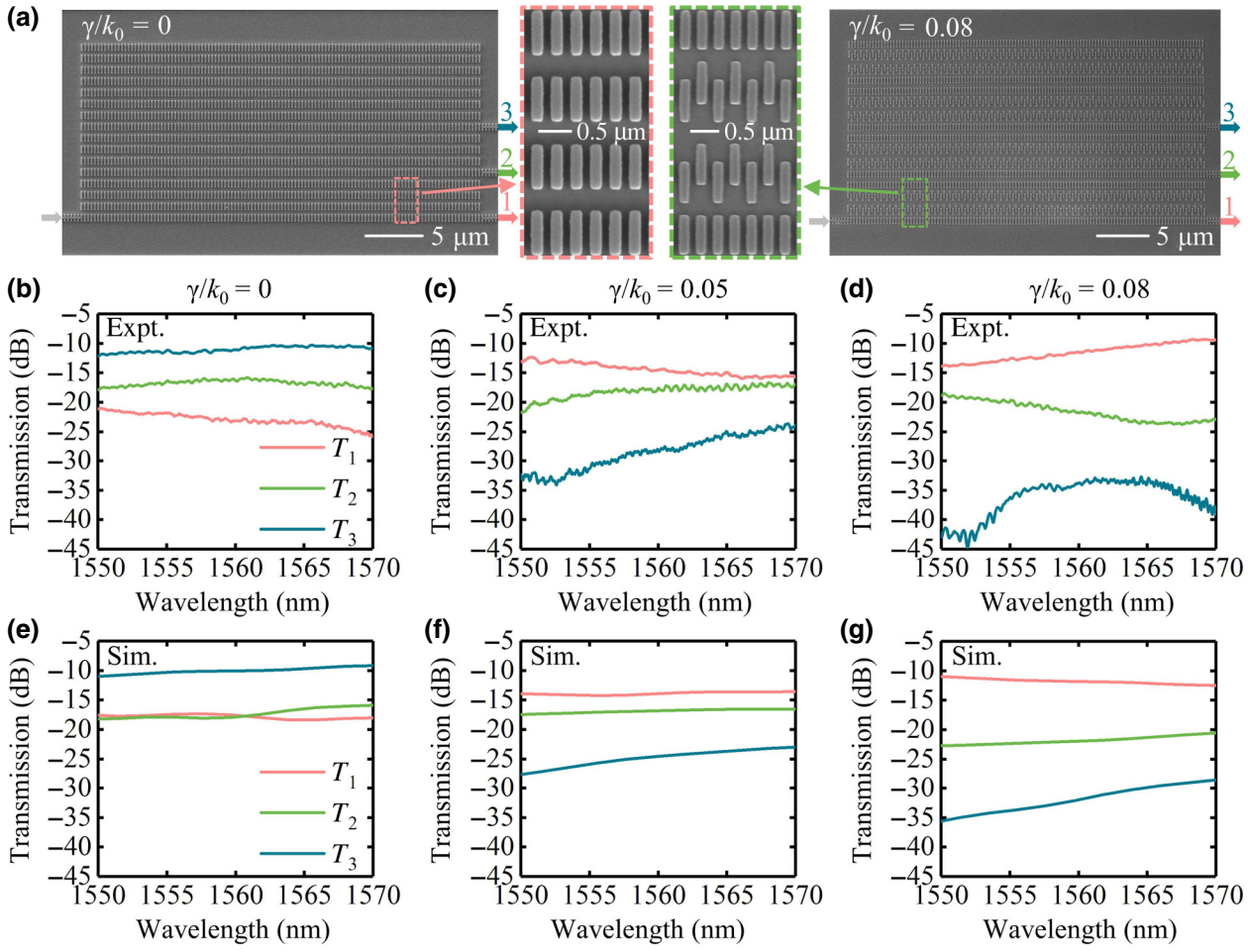

FIG. 4. The experimental and simulated transmission spectra of the fabricated APT-symmetric SWG waveguide arrays. The top-view SEM images of the fabricated SWG waveguide arrays are displayed in (a). The experimental transmission spectra for $\gamma/k_0 = 0$, 0.05, and 0.08 are shown in (b)–(d), respectively. The simulated transmission spectra for the same loss coefficients are shown in (e)–(g). In each case, the transmittance is measured with input injection from the lowest waveguide and output at three waveguides (A_1, A_2, and A_3) as shown in (a), and is represented by T_1, T_2, and T_3, respectively.

will have a certain bandwidth. Here, combined with the experimental results, the displayed wavelength range is 1550–1570 nm.

Figures 4(b)–4(d) display the optical transmission spectrum in experiments for non-Hermiticity γ/k_0 of 0, 0.05, and 0.08, respectively. Figures 4(e)–4(g) show the FDTD simulation results of Figs. 4(b)–4(d). As shown in Fig. 4(b), T_3 dominates the output signal strength, followed by T_2 and then T_1, which indicates that the light field has been diffracted into the array and has not been formed in the boundary region, that is, there is no edge states, which is consistent with the simulation results in Fig. 4(e). When the non-Hermiticity crosses the phase-transition point, the topological edge states will appear, as shown in Fig. 4(c), where T_1 dominates the output signal strength, followed by T_2 and then T_3. The corresponding simulation results in Fig. 4(f) also verify the topological phase-transition process. If we continue to increase the non-Hermiticity, we will see that the edge states are more localized with lower transmission loss. By comparing the results in Figs. 4(c) and 4(d), the loss-enhanced topological responses can be seen from the higher T_1, and the greater spacings between T_1 and T_2, T_2 and T_3, as shown in Figs. 4(d) and 4(g). The results of simulations and experiments are consistent both in the transmission efficiency and in the trend of changing with non-Hermiticity, which indicates that we have successfully implemented the non-Hermiticity modulated topological edge states in the on-chip APT-symmetric SWG waveguide arrays.

VI. CONCLUSION

In summary, the study has successfully demonstrated the realization of loss-modulated photonic topological edge states in on-chip anti-parity-time-symmetric waveguide arrays. The modulation effect induced by loss has been shown to not only induce topological phase transition but also enhance topological responses, resulting in a greater degree of localization of the topological edge states and anomaly reduced intrinsic loss. This work is significant because it contributes to the study of non-Hermitian control of passive photonic topological systems and has potential applications in topological lasing and topological optical switching. Furthermore, the passive SWG waveguide system developed in this study provides a platform for exploring various exotic non-Hermiticity-induced on-chip photonic topological phases and for investigating the physics and applications of various non-Hermitian topology systems with different models in the optical band, such as non-Hermitian induced Thouless pumping.

ACKNOWLEDGMENTS

This work is supported by the National Natural Science Foundation of China (61975062, U21A20511), and the Innovation Fund of Wuhan National Laboratory for Optoelectronics (WNLO), China.

[1] M. Z. Hasan and C. L. Kane, Colloquium: topological insulators, Rev. Mod. Phys. **82**, 3045 (2010).
[2] A. Bansil, H. Lin, and T. Das, Colloquium: Topological band theory, Rev. Mod. Phys. **88**, 021004 (2016).
[3] T. Ozawa, H. M. Price, A. Amo, N. Goldman, M. Hafezi, L. Lu, M. C. Rechtsman, D. Schuster, J. Simon, and O. Zilberberg, *et al.*, Topological photonics, Rev. Mod. Phys. **91**, 015006 (2019).
[4] H. Xue, Y. Yang, and B. Zhang, Topological acoustics, Nat. Rev. Mater. **7**, 974 (2022).
[5] Z. Wang, Y. Chong, J. D. Joannopoulos, and M. Soljačić, Observation of unidirectional backscattering-immune topological electromagnetic states, Nature **461**, 772 (2009).
[6] A. Blanco-Redondo, B. Bell, D. Oren, B. J. Eggleton, and M. Segev, Topological protection of biphoton states, Science **362**, 568 (2018).
[7] O. Zilberberg, S. Huang, J. Guglielmon, M. Wang, K. P. Chen, Y. E. Kraus, and M. C. Rechtsman, Photonic topological boundary pumping as a probe of 4D quantum hall physics, Nature **553**, 59 (2018).
[8] K. Kawabata, K. Shiozaki, M. Ueda, and M. Sato, Symmetry and topology in non-hermitian physics, Phys. Rev. X **9**, 041015 (2019).
[9] L. Feng, R. El-Ganainy, and L. Ge, Non-hermitian photonics based on parity–time symmetry, Nat. Photonics **11**, 752 (2017).
[10] S. Yao and Z. Wang, Edge states and topological invariants of non-hermitian systems, Phys. Rev. Lett. **121**, 086803 (2018).
[11] S. Weidemann, M. Kremer, T. Helbig, T. Hofmann, A. Stegmaier, M. Greiter, R. Thomale, and A. Szameit, Topological funneling of light, Science **368**, 311 (2020).
[12] C. Poli, M. Bellec, U. Kuhl, F. Mortessagne, and H. Schomerus, Selective enhancement of topologically induced interface states in a dielectric resonator chain, Nat. Commun. **6**, 6710 (2015).
[13] S. Weimann, M. Kremer, Y. Plotnik, Y. Lumer, S. Nolte, K. G. Makris, M. Segev, M. C. Rechtsman, and A. Szameit, Topologically protected bound states in photonic parity–time-symmetric crystals, Nat. Mater. **16**, 433 (2017).
[14] Y. Li, C. Liang, C. Wang, C. Lu, and Y.-C. Liu, Gain-loss-induced hybrid skin-topological effect, Phys. Rev. Lett. **128**, 223903 (2022).
[15] W. Zhu and J. Gong, Hybrid skin-topological modes without asymmetric couplings, Phys. Rev. B **106**, 035425 (2022).
[16] P. St-Jean, V. Goblot, E. Galopin, A. Lemaître, T. Ozawa, L. Le Gratiet, I. Sagnes, J. Bloch, and A. Amo, Lasing in topological edge states of a one-dimensional lattice, Nat. Photonics **11**, 651 (2017).
[17] M. Parto, S. Wittek, H. Hodaei, G. Harari, M. A. Bandres, J. Ren, M. C. Rechtsman, M. Segev, D. N. Christodoulides,

and M. Khajavikhan, Edge-mode lasing in 1D topological active arrays, Phys. Rev. Lett. **120**, 113901 (2018).
[18] H. Zhao, P. Miao, M. H. Teimourpour, S. Malzard, R. El-Ganainy, H. Schomerus, and L. Feng, Topological hybrid silicon microlasers, Nat. Commun. **9**, 981 (2018).
[19] C. Han, M. Lee, S. Callard, C. Seassal, and H. Jeon, Lasing at topological edge states in a photonic crystal l3 nanocavity dimer array, Light: Sci. Appl. **8**, 40 (2019).
[20] K. Takata and M. Notomi, Photonic topological insulating phase induced solely by gain and loss, Phys. Rev. Lett. **121**, 213902 (2018).
[21] C. Yuce, Stable topological edge states in a non-hermitian four-band model, Phys. Rev. A **98**, 012111 (2018).
[22] X.-W. Luo and C. Zhang, Higher-order topological corner states induced by gain and loss, Phys. Rev. Lett. **123**, 073601 (2019).
[23] H. Xue, Q. Wang, B. Zhang, and Y. D. Chong, Non-hermitian dirac cones, Phys. Rev. Lett. **124**, 236403 (2020).
[24] Y.-J. Wu, C.-C. Liu, and J. Hou, Wannier-type photonic higher-order topological corner states induced solely by gain and loss, Phys. Rev. A **101**, 043833 (2020).
[25] H. Wu, L. Jin, and Z. Song, Topology of an anti-parity-time symmetric non-hermitian Su-Schrieffer-Heeger model, Phys. Rev. B **103**, 235110 (2021).
[26] H. T. Teo, H. Xue, and B. Zhang, Topological phase transition induced by gain and loss in a photonic Chern insulator, Phys. Rev. A **105**, 053510 (2022).
[27] J.-R. Li, L.-L. Zhang, W.-B. Cui, and W.-J. Gong, Topological properties in non-hermitian tetratomic Su-Schrieffer-Heeger lattices, Phys. Rev. Res. **4**, 023009 (2022).
[28] H. Gao, H. Xue, Q. Wang, Z. Gu, T. Liu, J. Zhu, and B. Zhang, Observation of topological edge states induced solely by non-hermiticity in an acoustic crystal, Phys. Rev. B **101**, 180303 (2020).
[29] H. Gao, H. Xue, Z. Gu, T. Liu, J. Zhu, and B. Zhang, Non-hermitian route to higher-order topology in an acoustic crystal, Nat. Commun. **12**, 1888 (2021).
[30] S. Liu, S. Ma, C. Yang, L. Zhang, W. Gao, Y. J. Xiang, T. J. Cui, and S. Zhang, Gain- and loss-induced topological insulating phase in a non-hermitian electrical circuit, Phys. Rev. Appl. **13**, 014047 (2020).
[31] H. Fan, H. Gao, S. An, Z. Gu, S. Liang, Y. Zheng, and T. Liu, Hermitian and non-hermitian topological edge states in one-dimensional perturbative elastic metamaterials, Mech. Syst. Signal. Process. **169**, 108774 (2022).
[32] G. Xu, Y. Yang, X. Zhou, H. Chen, A. Alù, and C.-W. Qiu, Diffusive topological transport in spatiotemporal thermal lattices, Nat. Phys. **18**, 450 (2022).
[33] Z. Gao, S. T. Fryslie, B. J. Thompson, P. S. Carney, and K. D. Choquette, Parity-time symmetry in coherently coupled vertical cavity laser arrays, Optica **4**, 323 (2017).
[34] H. Zhao, X. Qiao, T. Wu, B. Midya, S. Longhi, and L. Feng, Non-hermitian topological light steering, Science **365**, 1163 (2019).
[35] A. Blanco-Redondo, I. Andonegui, M. J. Collins, G. Harari, Y. Lumer, M. C. Rechtsman, B. J. Eggleton, and M. Segev, Topological optical waveguiding in silicon and the transition between topological and trivial defect states, Phys. Rev. Lett. **116**, 163901 (2016).
[36] Q. Liu, S. Li, B. Wang, S. Ke, C. Qin, K. Wang, W. Liu, D. Gao, P. Berini, and P. Lu, Efficient mode transfer on a compact silicon chip by encircling moving exceptional points, Phys. Rev. Lett. **124**, 153903 (2020).
[37] W. Liu, Y. Zhang, Z. Deng, J. Ye, K. Wang, B. Wang, D. Gao, and P. Lu, On-chip chiral mode switching by encircling an exceptional point in an anti-parity-time symmetric system, Laser Photonics Rev. **16**, 2100675 (2022).
[38] M. Pan, H. Zhao, P. Miao, S. Longhi, and L. Feng, Photonic zero mode in a non-hermitian photonic lattice, Nat. Commun. **9**, 1308 (2018).
[39] See Supplemental Material at http://link.aps.org/supplemental/10.1103/PhysRevApplied.20.044019 for the symmetry of the Hamiltonian, the numerical calculation of the Zak phase, the derivation of exact solution of edge states, the effect of disorder on topological edge states, the simulation details, and the mode excitation.
[40] Q. Cheng, Y. Pan, Q. Wang, T. Li, and S. Zhu, Topologically protected interface mode in plasmonic waveguide arrays, Laser. Photon. Rev. **9**, 392 (2015).